Isotropic and intrinsic orbital current generation in epitaxial vanadium films

Hui Zhang [1], Haoyu Lin [1], Kun Zheng [1], Yangping Wang,[2] Zheng Li,[1] Jie Xu [3], Jing Meng,[1] Changjun Jiang,[3] Dongmei Jiang,[1] Tian Shang [1,4], Qingfeng Zhan [1,4,*] and Yang Xu [1,4,†]

[1] *School of Physics, East China Normal University, Shanghai 200241, China*
[2] *College of Physics and Electronic Engineering, Nanyang Normal University, Nanyang 473061, China*
[3] *Key Laboratory for Magnetism and Magnetic Functional Materials of the Ministry of Education, Lanzhou University, Lanzhou 730000, China*
[4] *Key Laboratory of Polar Materials and Devices (MOE), East China Normal University, Shanghai 200241, China*

(Received 16 April 2026; revised 6 August 2026; accepted 7 August 2026; published 2 September 2026)

It has been suggested that the anisotropic behavior of orbital transport can be distinct from that of the spin counterpart. On another front, the microscopic mechanisms underlying the anomalous Hall effect and the spin Hall effect are generally categorized into the intrinsic Berry curvature mechanism and the extrinsic mechanism induced by disorder scattering, each with distinct scaling relations. A similar analysis for orbital transport has rarely been performed. Here, we investigate both aspects of the orbital current generation in a light metal V. The orbital-to-spin conversion is achieved using a heavy metal Pt insertion layer or Ni as the ferromagnetic layer. Benefiting from the epitaxial growth of V with a low disorder strength, the orbital current generation is characterized by a large transverse conductivity and long diffusion length, consistent with the expectation for an intrinsic orbital Hall effect. Across all the heterostructures studied, we confirm the orbital current's isotropic nature, i.e., the orbital current generation is barely affected when the charge current is applied along different crystallographic directions, consistent with the high-symmetry crystal structure. Crucially, the intrinsic nature of the orbital current generation is demonstrated by the scaling analysis, showing a scattering-independent orbital Hall conductivity.

DOI: 10.1103/6ql2-m6bq

I. INTRODUCTION

Symmetry breaking, a common thread in physics, can render spatial directions inequivalent, leading to anisotropy. In the context of spintronics, magnetizations, spin polarizations, and orbital textures, etc., naturally select preferred directions, laying the foundation for anisotropic transport phenomena of technological significance [1]. Taking magnetic random-access memory as an example, the initial versions utilizing giant/tunneling magnetoresistance exploit anisotropic electron scattering that depends on the relative orientation of the magnetization in different ferromagnetic (FM) layers [2]; While in the latest generations, exotic mechanisms for spin-orbit torque generation are currently under intensive research [3–5]. A pertinent example is altermagnets generating spin-splitting torque depending on the applied electrical current relative to specific crystallographic directions, where the resultant spin polarization of the spin current can be collinear with the Néel vector [6,7]. Another notable example is that the concerted action of conventional and magnetic spin Hall effects can lead to anisotropic spin current generation even in a high-symmetry cubic noncollinear antiferromagnet [8].

Long assumed to be quenched by the crystal field, the orbital degree of freedom has been recently argued to be a more fundamental source of nonequilibrium angular momentum than spin, when the electronic band structure is characterized by varying orbital characters across the momentum space via, e.g., the orbital Hall effect (OHE) [9–11]. In contrast to the spin counterpart, the anisotropy of orbital angular momentum transport has received less attention, although the anisotropy can generally be expected considering the anisotropic probability distribution represented by most orbitals and the hybridization between them. Indeed, several experimental findings implicated the existence of such anisotropy. For example, the difference in the characteristic length scale of orbital torque generation in atomically ordered $L1_1$-CoPt and disordered A1-CoPt alloys was argued to correlate with the anisotropic in-plane and out-of-plane hybridization between the Co and Pt *d* orbitals [12]. Furthermore, the orbital torque efficiency was found to be significantly higher in fcc Ti(001) than Ti(111) when they are, respectively, interfaced with a fcc (111) FM, which was attributed to the different alignment conditions between the momentum-space orbital Berry curvature hotspots [13].

In the above works, however, the anisotropy manifests more as a property of the orbital-torque-probing FM layer, or as a characteristic of the specific combination of the orbital current source and the FM layer. The anisotropy of orbital current generation in the source layer itself has rarely been explored. A theoretical study predicted significant anisotropy in the OHE of light metals with a relatively low-symmetry hexagonal close-packed structure; i.e., the orbital Hall

*Contact author: qfzhan@phy.ecnu.edu.cn
†Contact author: yxu@phy.ecnu.edu.cn

conductivity differs substantially when the driving charge current is applied along different crystallographic directions. The anisotropy of the OHE was also found to be distinct from the spin Hall effect, although both share identical symmetry transformation properties [14]. The experimental effort along this line was limited to interfacial effects and insulating source layers: Anisotropic orbital Rashba-Edelstein effect was recently demonstrated in epitaxial CuO films, with a fourfold symmetry comprehensible only when the induced crystal distortion is considered [15]. The anisotropies of the orbital and spin angular momentum can be distinctly different due to fundamental differences in the chiral structures of various bands, which can be sensitive to the position of the Fermi level in a multiorbital system. This was showcased by the two-dimensional electron gas at the $LaAlO_3/SrTiO_3$ interface, where the orbital response is isotropic while the spin component is anisotropic [16].

These findings highlight a central challenge in understanding the anisotropy of orbital current generation: the response function's anisotropy cannot be naively inferred from the underlying crystal symmetry without a detailed analysis of how weighted contributions from bands with different orbital characters add up. Choosing a high-symmetry source material, such as one with a cubic structure, is expected to partially alleviate this difficulty. On another front, it has been proposed that disorder plays a critical role in the relaxation of nonequilibrium orbital densities, and the consideration of extrinsic mechanisms may be vital in addressing the discrepancy between theory and experimental results in OHE materials, especially in thin films of light metal, such as Ti [17–20]. Therefore, differentiating the intrinsic versus extrinsic mechanisms underlying the orbital transport is also of primary importance.

In this work, we investigate the orbital current generation in a light metal V with a bcc structure, which was predicted to exhibit a large orbital Hall conductivity $\sigma_{OH} \sim 5.8 \times 10^3(\hbar/e)(\Omega\,\mathrm{cm})^{-1}$ and a spin counterpart $\sigma_{SH} \sim -9 \times 10^1(\hbar/e)(\Omega\,\mathrm{cm})^{-1}$ [21]. Utilizing a heavy metal Pt insertion layer or Ni as the FM layer for the orbital-to-spin current conversion, we achieve a dampinglike torque efficiency on the order of 0.1, corresponding to $\sigma_{OH} \sim 1.8 \times 10^3(\hbar/e)(\Omega\,\mathrm{cm})^{-1}$. By varying the V layer thickness, we determine the orbital diffusion length to be $\lambda_{orb} \sim 5.38$ nm. Benefiting from the reduced scattering in our high-quality epitaxial V films, the σ_{OH} is orders of magnitude higher than ever reported [22–25], and on the same order as the expected value for intrinsic OHE from first-principles calculations [21]. Crucially, compared with previous studies on amorphous V films, our single-crystal films enable the application of electrical current along different crystallographic directions. We confirm the isotropy of orbital current generation in V, which is consistent with the expectation for cubic materials. Characterizing the orbital current generation at different temperatures, we found a scattering-independent scaling, consistent with the expectation for intrinsic OHE.

II. EXPERIMENTAL METHODS

Samples of V/Ni, V/Pt/Py (Permalloy, $Ni_{81}Fe_{19}$), V/Pt/Py/Pt, and $V/[Co/Pt]_3$ heterostructures were deposited

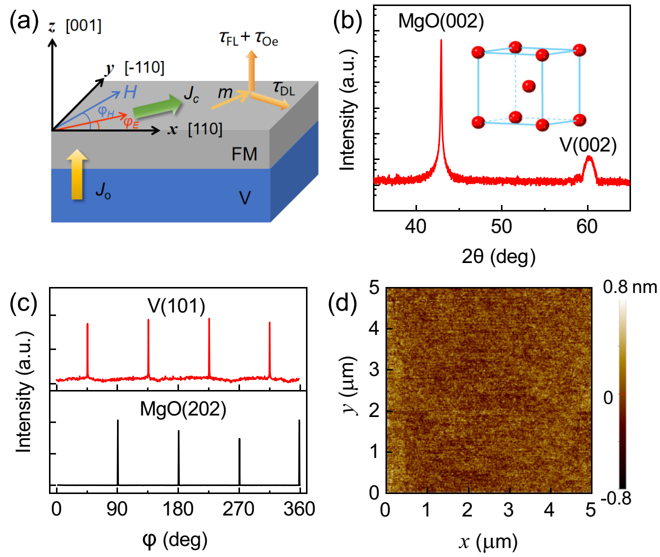

FIG. 1. (a) A schematic of the orbital current generation and detection in a V/FM bilayer by ST-FMR measurements. Via the OHE of V, an in-plane microwave current generates an orbital current, which exerts torques on the FM magnetization after being converted to a spin current in the FM layer, or via a heavy-metal insertion layer before entering the FM layer (not shown). (b) High-resolution XRD θ–2θ spectrum of a V single-layer film grown on the MgO(001) substrate. The inset illustrates the bcc structure of V. (c) The ϕ-scan around V(101), showing a 45° epitaxial relation with the substrate. (d) The surface morphology of V, characterized by AFM.

on MgO(001) single-crystal substrates by DC magnetron sputtering with a base pressure below 5×10^{-8} Torr. The MgO(001) substrate was first pre-annealed at 600 °C for 1 h under ultrahigh-vacuum conditions to remove surface contaminants. Epitaxial V films were then deposited at 300 °C with a V target (99.99% purity) at a sputtering power of 30 W and Ar gas pressure of 3×10^{-3} Torr, followed by postannealing at 300 °C for 1 h to enhance crystallinity. Ni, Py, Co, and Pt layers were deposited at room temperature using sputtering powers of 30 W for Ni and Py, and 20 W for Co and Pt, respectively. The crystallinity of the V films was characterized by high-resolution X-ray diffraction (XRD, Bruker D8 Discover) with Cu $K_{\alpha1}$ radiation ($\lambda = 1.5406$ Å), including θ-2θ scans and ϕ scans. The surface morphology was measured by atomic force microscopy (AFM, Park NX10) in noncontact mode. Static magnetic properties were tested using a magnetic property measurement system (Quantum Design). Spin-torque ferromagnetic resonance (ST-FMR) measurements were performed using a vector network analyzer (Keysight N5232B) at microwave frequencies of 6–14 GHz, with a low-frequency (277 Hz) ac magnetic field (0.2 mT) for signal modulation. The radio frequency source output power was set to 15–20 dBm, and the resonance response was verified to be in the linear regime. The measurement scheme for ST-FMR is shown in Fig. 1(a). While in typical ST-FMR measurements only the orientation of the magnetic field is varied, here the microwave current is also applied along different crystallographic directions to study orbital current anisotropy. In other words, ϕ_H is scanned from 0° to 360° in the film

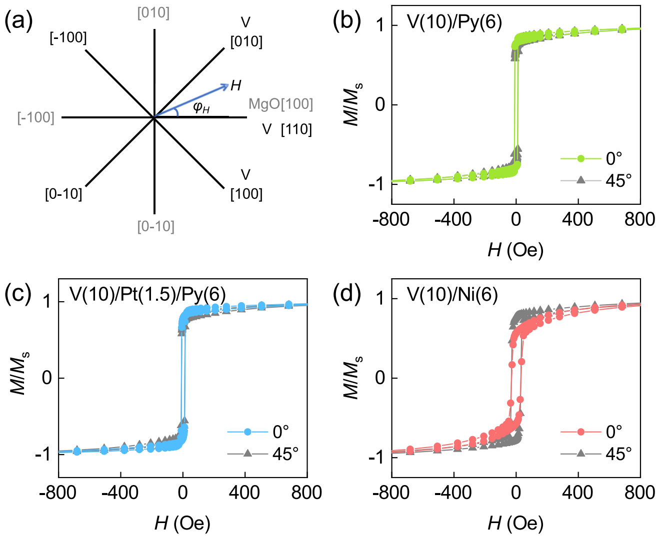

FIG. 2. (a) Schematic diagram of the crystallographic orientations of V and MgO in the (001) plane, and the direction of the in-plane magnetic field, at an angle ϕ_H with respect to the V[110] direction. (b)–(d) respectively shows the M–H loops of V/Py, V/Pt/Py, and V/Ni measured at $\phi_H = 0^\circ$ and 45°. Except for V/Ni, the magnetization loops are basically isotropic along different in-plane directions. For V/Ni, the slanted loop at $\phi_H = 45^\circ$ can be attributed to an anisotropy due to an induced epitaxy at the interface. The numbers in the parentheses indicate the thickness of the corresponding layer in nm.

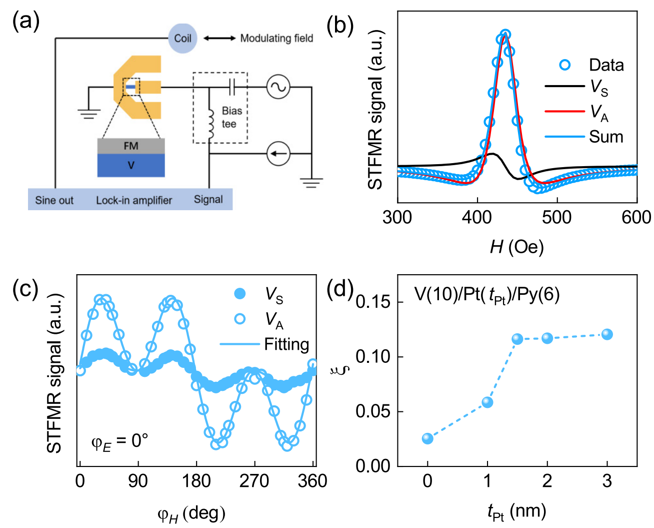

FIG. 3. (a) A schematic illustration of the field-modulated ST-FMR measurement setup. A microwave and a dc current are applied via a bias tee, while a coil modulates the applied field at a low frequency. (b) The ST-FMR spectrum of V(10)/Pt(1.5)/Py(6) with microwave frequency at 6 GHz. The black and red curves show the antisymmetric and symmetric Lorentzian components of the resonance peak, respectively. Note that the antisymmetric component is labeled V_S while the symmetric one is labeled V_A (see the main text). (c) In-plane magnetic field angle ϕ_H dependence of V_S and V_A for V(10)/Pt(1.5)/Py(6) with the microwave current applied along V[110]($\phi_E = 0^\circ$). The solid lines show the fitting to $\cos\phi_H \sin 2\phi_H$. (d) The torque efficiency ξ as a function of the Pt layer thickness $t_{\rm Pt}$ for V(10)/Pt($t_{\rm Pt}$)/Py(6).

plane for each fixed value of ϕ_E. The Hall resistance was measured in a physical property measurement system (PPMS, Quantum Design) with a dc source and lock-in amplifier. The current-induced magnetization measurements were conducted using a Keithley 6221 current source and a 2182 nanovoltmeter.

III. RESULTS

Figure 1(b) shows the high-resolution XRD θ-2θ spectrum of a V single-layer film grown on MgO(001). The (00l) peaks reveal the film growth orientation and confirm the body-centered cubic structure of V. As shown in Fig. 1(c), the ϕ scan of V(101) exhibits fourfold symmetry, with the V peaks shifted by 45° relative to the MgO peaks, indicating the epitaxial relation of MgO(001)[100] ∥ V(001)[110] [also shown in Fig. 2(a)]. The smooth surface of the V film is evidenced by a rms roughness of 0.20 nm over an AFM measurement area of $5 \times 5\ \mu m^2$ [Fig. 1(d)]. These characterizations confirm the high-quality and single-crystal nature of our epitaxial V films.

The orbital current generated in V must be converted to a spin current before it can interact with the magnetization in the adjacent FM layer and then be detected. For efficient detection by ST-FMR, Py is chosen as the FM layer due to its large anisotropic magnetoresistance. A heavy-metal Pt layer is inserted between V and Py for orbital-to-spin conversion. Alternatively, we use Ni as the FM layer, which is an ideal orbital-to-spin converter due to its large spin-orbit correlation at the Fermi level [26,27]. We first characterize the static magnetic properties of these heterostructures, with a magnetic field applied in the (001) plane and at $\phi_H = 0^\circ$ and 45° with respect to the V[110] direction. The magnetization loops for V/Py, V/Pt/Py, and V/Ni are shown in Figs. 2(b)–2(d), respectively. The rectangular shape of the loops and the clear hysteresis confirm the easy-plane anisotropy of these heterostructures, a prerequisite for ST-FMR measurements. Importantly, no anisotropy can be observed for the loops measured with different ϕ_H. The only exception is V/Ni, for which the loop at $\phi_H = 0^\circ$ shows a slanted shape and a reduced remanence ratio of $M_r/M_s \sim 0.56$ compared to 0.76 at $\phi_H = 45^\circ$. Such anisotropy might be due to an induced epitaxy at the interface [28].

ST-FMR has been established as a powerful probe of orbital/spin torques [29]. In a typical ST-FMR setup, the signal is a rectified voltage $V_{\rm mix}$, whose line shape can be decomposed into a symmetric and an antisymmetric component near the resonant condition, characterizing the in-plane spin-orbit torque $\tau_\parallel$ and out-of-plane torque $\tau_\perp$, respectively. In this work, we employed a field-modulated ST-FMR technique [Fig. 3(a)] to suppress large nonmagnetic background signals, yielding a $dV_{\rm mix}/dH$ signal. As mentioned above, Py is an ideal FM layer for ST-FMR measurements due to its large anisotropic magnetoresistance. However, due to the small $\sigma_{\rm SH}$ of V and the inefficiency of Py in orbital-to-spin conversion, we exploit the strong spin-orbit coupling of a heavy-metal Pt insertion layer [26,30]. A representative ST-FMR spectrum for V(10)/Pt(1.5)/Py(6) (thickness in nm) is shown in Fig. 3(b). The signal can be decomposed into symmetric and antisymmetric Lorentzian components using Eq. (1) [31–33]:

$$dV_{\rm mix}/dH = \frac{-2V_{\rm S}\Delta^2(H-H_{\rm r}) + V_{\rm A}\Delta[\Delta^2-(H-H_{\rm r})^2]}{[(H-H_{\rm r})^2+\Delta^2]^2}. \tag{1}$$

Note that due to the derivative nature of the signal in our field-modulated mode, the antisymmetric Lorentzian component corresponds to $V_{\rm S}$ while the symmetric Lorentzian one to $V_{\rm A}$. The decomposition is corroborated by the ϕ_H dependence of $V_{\rm S}$ and $V_{\rm A}$ shown in Fig. 3(c), with both showing a $\cos\phi_H \sin 2\phi_H$ dependence consistent with the expectation for a conventional spin current with only y polarization. The charge-to-spin conversion efficiency ξ is calculated by Eq. (2) [33,34]:

$$\xi = \frac{V_{\rm S}}{V_{\rm A}}\frac{e}{\hbar}\mu_0 M_{\rm s} t_{\rm FM} t_{\rm NM}\sqrt{1+\frac{4\pi M_{\rm eff}}{H_{\rm r}}}. \tag{2}$$

In Eqs. (1) and (2), $H_{\rm r}$ is the resonance field, Δ is the half width at half maximum, μ_0 is the vacuum permeability, $t_{\rm FM}$ ($t_{\rm NM}$) is the thickness of the FM (nonmagnetic) layer, $M_{\rm s}$ is the saturation magnetization, and $M_{\rm eff}$ is the effective magnetization, which can be obtained from the Kittel equation $f = \frac{\gamma}{2\pi}\sqrt{(H_{\rm r}+H_{\rm k})(H_{\rm r}+4\pi M_{\rm eff}+H_{\rm k})}$, where $H_{\rm k}$ is the magnetocrystalline anisotropy field. We found that as the thickness of Pt is increased, ξ increases first before saturating at $t_{\rm Pt} \geqslant 1.5$ nm, consistent with the spin diffusion length of Pt [35–37]. Therefore, in the following experiments on V/Pt/Py heterostructures, we fix $t_{\rm Pt}$ at 1.5 nm.

Measurements of ξ as a function of $t_{\rm FM}$ allow us to separately estimate the dampinglike ($\xi_{\rm DL}$) and fieldlike ($\xi_{\rm FL}$) torque efficiencies by Eq. (3) [33,34]:

$$\frac{1}{\xi} = \frac{1}{\xi_{\rm DL}}\left(1+\frac{\hbar}{e}\frac{\xi_{\rm FL}}{\mu_0 M_{\rm s} t_{\rm FM} t_{\rm NM}}\right), \tag{3}$$

which shows that the intercept of $1/\xi$ in the limit of $1/t_{\rm FM} \to 0$ yields $\xi_{\rm DL}$. We focus on $\xi_{\rm DL}$, which is the main driving force in many application scenarios of the spin/orbital current, e.g., magnetization switching. For V(10)/Pt(1.5)/Py($t_{\rm Py}$), $\xi_{\rm DL} = 0.176$ is obtained. This large value of $\xi_{\rm DL}$ mainly comes from the orbital current generated in V, which is efficiently converted to a spin current by Pt and then exerts a large torque on the magnetization of Py. To compensate for the spin current generated by the Pt layer itself, we also fabricated V(10)/Pt(1.5)/Py($t_{\rm Py}$)/Pt(1.5), in which the spin Hall contribution from Pt is canceled due to the symmetric configuration. $\xi_{\rm DL}$ indeed decreases, but still retains a large value of 0.124. Notably, the positive sign of $\xi_{\rm DL}$ is consistent with a dominant orbital contribution according to first-principles calculations [21].

Next, we investigate the anisotropy of the spin current converted from the orbital current of V. This is achieved by varying the direction of the microwave current relative to the crystallographic orientation of V, i.e., changing ϕ_E. For each fixed ϕ_E, by ϕ_H-scanning measurements, as shown in Fig. 3(c), we obtain the values of $V_{\rm S}$ and $V_{\rm A}$ from a fitting to the $\cos\phi_H \sin 2\phi_H$ angular dependence. ξ can then be determined using Eq. (2). As shown in Figs. 4(c) and 4(d), for both V(10)/Pt(1.5)/Py(6) and V(10)/Pt(1.5)/Py(6)/Pt(1.5), ξ shows a negligible variation when ϕ_E traverses 90° from V[110].

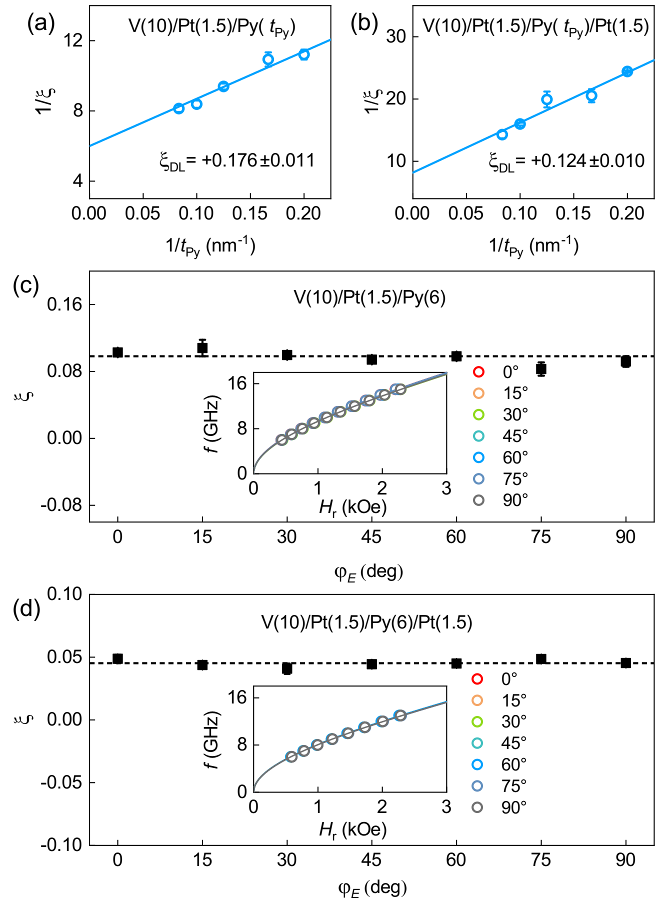

FIG. 4. $1/\xi$ as a function of $1/t_{\rm Py}$ in V(10)/Pt(1.5)/Py($t_{\rm Py}$) (a) and V(10)/Pt(1.5)/Py($t_{\rm Py}$)/Pt(1.5) (b). The solid line shows a linear fit. The anisotropy of the orbital current generation, characterized by ξ as a function of ϕ_E, is shown in (c) for V(10)/Pt(1.5)/Py(6) and (d) for V(10)/Pt(1.5)/Py(6)/Pt(1.5). The insets plot the resonance frequency f as a function of the resonance field $H_{\rm r}$, where the overlapping lines with different ϕ_E indicate the isotropy of the magnetism of Py, echoing the results in Fig. 2.

The isotropy of the magnetism of Py has been confirmed in Figs. 2(b) and 2(c), and is also reflected by the overlapping lines in the insets of Figs. 4(c) and 4(d). The spin-orbit correlation of Pt is also isotropic [8,38,39]. Therefore, the isotropy of ξ confirms the isotropic orbital current generation in V, which forms the main experimental finding of this work.

The efficient and isotropic orbital current generation in V is also verified using Ni as the FM layer, where orbital-to-spin conversion and spin-torque absorption occur simultaneously. Varying the Ni thickness in V(10)/Ni($t_{\rm Ni}$), we obtain a large $\xi_{\rm DL} = 0.122$ [Fig. 5(a)], corresponding to $\sigma_{\rm OH} = \xi_{\rm DL}/\rho_{xx} = 1.8\times10^3(\hbar/e)(\Omega\,{\rm cm})^{-1}$ (with $\rho_{xx} \sim 32.94$ μΩ cm). Note that here we have assumed a perfect transmission of the orbital current at the interfaces. In reality, the transparency is bound to be less than 1, which translates to an even larger $\sigma_{\rm OH}$. This indicates not only a high efficiency of orbital current generation in V but also a conversion efficiency of Ni as high as that of a Pt insertion layer. We also vary the thickness of V while keeping the thickness of Ni constant. As shown in Fig. 5(b), ξ increases with $t_{\rm V}$ first and then tends to saturate.

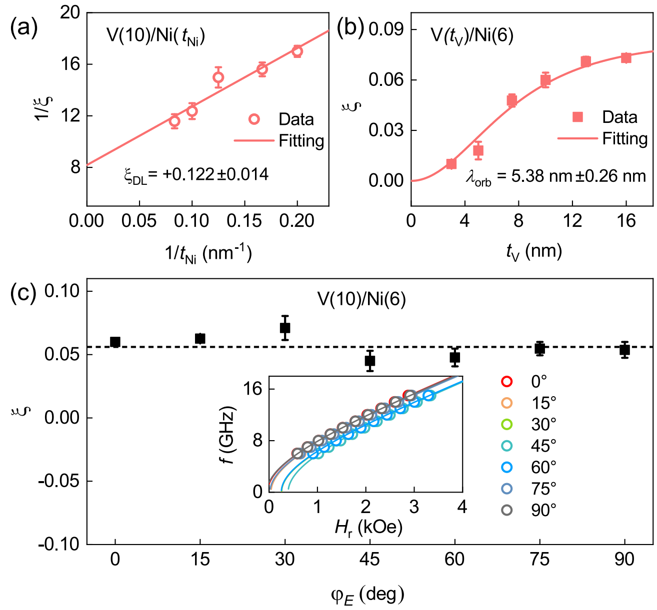

FIG. 5. (a) $1/\xi$ as a function of $1/t_{Ni}$ in V(10)/Ni(t_{Ni}). The solid line shows a linear fit. (b) ξ as a function of t_V in V(t_V)/Ni(6). The solid line shows the fitting to a drift-diffusion equation (4). (c) ξ as a function of ϕ_E for V(10)/Ni(6). The inset shows the slight in-plane anisotropy of the Ni magnetism as reflected by the nonoverlapping lines, echoing the results in Fig. 2.

The orbital diffusion length λ_{orb} can be obtained by fitting ξ as a function of t_V to a drift-diffusion equation [17,40]:

$$\xi(t_V) = \xi_\infty\left[1 - \text{sech}\left(\frac{t_V}{\lambda_{orb}}\right)\right], \qquad (4)$$

in which ξ_∞ is the value in the limit of an infinitely thick V. The fitting yields $\lambda_{orb} = 5.38$ nm. The increasing trend of ξ and the relatively large λ_{orb} indicate that the orbital current is generated in the bulk of V via the OHE. We exclude the effect of the self-torque in Ni by a control sample of Si/SiO_2/Ni/Si_3N_4, which shows negligible V_S in our ST-FMR measurements (not shown). Indeed, the self-torque of Ni is expected to manifest itself only when a thick Ni layer interfaces with a heavy metal layer [41,42].

The ϕ_E dependence of ξ shown in Fig. 5(c) is again basically isotropic. The ϕ_E dependence of ξ for various heterostructures shown in Figs. 4(c), 4(d), and 5(c), collectively allows us to reach the conclusion of isotropic orbital current generation in V.

To further confirm the isotropic nature of the orbital current, we performed current-induced magnetization switching experiments in V(10)/[Co(0.3)/Pt(0.7)]$_3$. The Hall resistance of the heterostructure with an out-of-plane magnetic field with the current along V[100] and V[110] is shown, respectively, in Figs. 6(a) and 6(b). The square loop originates from the anomalous Hall effect of the FM layer with perpendicular magnetic anisotropy. Current-induced magnetization switching under an in-plane auxiliary magnetic field is shown in Figs. 6(c) and 6(d). The cases for the current along different crystallographic directions show a consistent switching ratio of ∼88% and critical current density of 2.3×10^7 A cm^{-2}, comparable to the value reported previously

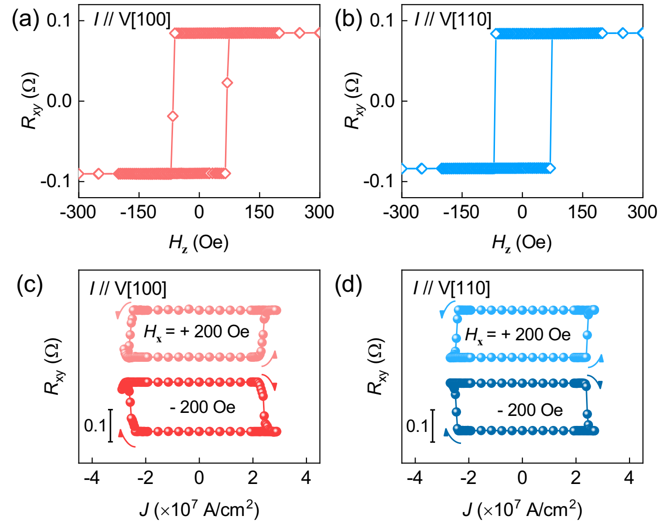

FIG. 6. The Hall resistance loops for V(10)/[Co(0.3)/Pt(0.7)]$_3$ are shown in (a) and (b), where the current is applied along V[100] and V[110], respectively. (c) and (d) present the current-induced magnetization switching under an in-plane auxiliary field of ± 200 Oe.

for V/CoFeB/MgO [22]. Notably, the current-induced magnetization switching properties show no dependence on the direction of the applied current, again confirming isotropic orbital current generation in V.

To investigate whether orbital current generation in V originates from intrinsic or extrinsic mechanisms, we performed ST-FMR measurements across a range of temperatures. Due to the good metallicity, the σ_{xx} of V can be tuned substantially by varying temperature (see the inset of Fig. 7). Since one needs ξ_{DL} for the extraction of σ_{OH}, and the determination of ξ_{DL} requires measurements on samples with varying FM layer

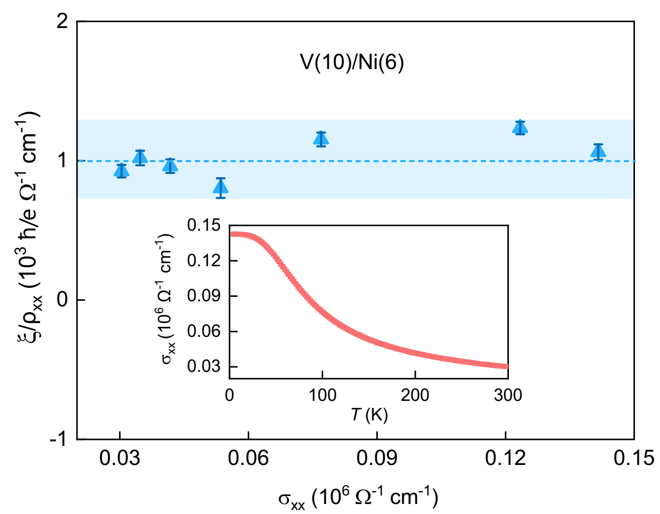

FIG. 7. The electrical conductivity σ_{xx} dependence of ξ/ρ_{xx}, as a measure of the orbital Hall conductivity σ_{OH}, for V(10)/Ni(6). The dashed line and the shaded area guide the eye for the constant behavior against variation in σ_{xx}. The inset shows the temperature dependence of σ_{xx} of the V(10) film.

TABLE I. Comparison of the orbital transport properties of V from various studies. For the first three rows, consideration of both the spin Hall and orbital Hall effects is essential. For the remaining rows, a dominant OHE is sufficient. For row 1, σ_{OH} should be treated as an effective σ_{SH}. For row 2, the small λ_{orb} results from fixing σ_{OH} to the first-principles calculation value when fitting the MOKE signal. In other words, the large σ_{OH} in row 2 is not an experimentally determined value. σ_{OH} takes a negative value for rows 1 and 7. For row 8, we assume a perfect transmission of the orbital current at the interfaces, and the σ_{OH} should be considered a lower bound of the true value. HH: harmonic Hall; MOKE: magneto-optical Kerr effect; ST-FMR: spin-torque ferromagnetic resonance; HMR: Hanle magnetoresistance.

Row	Method	$\lvert\sigma_{OH}\rvert$ $(\hbar/e)(\Omega\ \mathrm{cm})^{-1}$	λ_{orb} (nm)	ρ_{xx} ($\mu\Omega$ cm)	Ref.
1	HH	7.0×10^0		143	[22]
2	MOKE	2.1×10^3	0.7	41	[43]
3	MOKE	9.8×10^1	35	41	[43]
4	ST-FMR		3.6		[23]
5	HMR	7.8×10^1	2	270	[24]
6	HMR	6.3×10^1	2	380	[24]
7	ST-FMR	7.2×10^2	15	85	[25]
8	ST-FMR	1.8×10^3	5.4	33	this work

thickness, here we use ξ/ρ_{xx} as a measure of σ_{OH} for a sample with a fixed FM layer thickness. As shown in Fig. 7, ξ/ρ_{xx} is basically constant in our range of σ_{xx}, i.e., the orbital current generation in V is independent of scattering.

IV. DISCUSSIONS

Dominant OHE. A complex competition among the bulk spin Hall effect, OHE, and interfacial Rashba effect was suggested to be responsible for the sign reversal of ξ_{DL} with increasing V thickness in V/CoFeB/MgO [22]. The overall thickness dependence of the magneto-optical Kerr effect (MOKE) signal for thick V films can be accounted for only with two distinct length scales, indicating that invoking both the spin and orbital Hall effects is essential [43]. In contrast, a dominant OHE was concluded from previous measurements of ST-FMR, Hanle magnetoresistance, and THz emission [23–25]. The large and positive ξ_{DL} we obtained translates to a dominant σ_{OH} over σ_{SH}, consistent with the expectation from first-principles calculations [21]. This is further reflected in the single diffusion length extracted from Fig. 5(b), where the increasing-then-saturating trend also points to the bulk nature of the orbital current generation.

Magnitude of the OHE. The values of σ_{OH} extracted from various reports are listed in Table I. The small σ_{OH} value (with a negative sign) determined by harmonic Hall measurements on V/CoFeB/MgO heterostructures (row 1), is due to the cancellation between σ_{SH} and σ_{OH} [22]. For magneto-optical Kerr effect measurements (rows 2 and 3), σ_{OH} is a fitting parameter that covaries with λ_{orb} and is allowed to change in a large interval [43]. For the ST-FMR data shown in row 7, σ_{OH} takes a negative value, which was argued to be determined by the competition between local electron circulation and contributions that fundamentally originate in the circulation of Wannier functions at the surface of the sample [25]. The latter part is sensitive to the specific sample surfaces, and the relative weights of the two contributions depend on the position of the Fermi level. This might explain the differences in the sign for samples prepared by different groups.

The small σ_{OH} reported to date has consistently been attributed to disorder scattering in the V films, which are low in crystallinity or even amorphous, as evidenced by the large ρ_{xx} and, in some cases, absence of vanadium diffraction peaks [22,24]. We note that, in studies of spin/orbital current generation, epitaxial growth of V has been reported previously only in Ref. [22]. However, to ensure the perpendicular magnetic anisotropy of the FM layer, the samples studied there were actually in a thickness range where V is amorphous [22]. Benefiting from the epitaxial growth of high-quality V films, we are able to achieve a low ρ_{xx} and a large σ_{OH} on the same order of magnitude as the first-principles calculated value for the intrinsic OHE [21]. We remark that, in general, how the improved crystallinity might enhance σ_{OH} is not a trivial question and warrants further investigation. On the one hand, long orbital lifetimes rely on good crystallinity, as experimentally demonstrated at least in the context of orbital current filtering through a tunnel barrier [16,44,45]. On the other hand, early theoretical works suggest a σ_{OH} independent of ρ_{xx} in a moderately dirty regime [46]. Moreover, the enhanced crystallinity of both the source layer and the FM layer may impose a more stringent constraint on the matching of orbital Berry curvature hotspots, thereby diminishing σ_{OH} [13].

The orbital diffusion length. Our λ_{orb} value is in reasonable agreement with the reported values, which are also listed in Table I, and comparable to the value for other light metal orbital current source materials, such as Cr and Mn [47,48]. The large variation of λ_{orb} in rows 2 and 3 comes from the fact that the λ_{orb} and σ_{OH} are interdependent fitting parameters in MOKE data analysis [43], and the large σ_{OH} we obtained tends to favor the short side of this interval. We also note a first-principles calculation study suggesting the possibility of mistaking the spin diffusion length as λ_{orb} due to the spatially rapid orbital-to-spin current conversion [49], and an experimental report of a subnanometer λ_{orb} in heavy metals at the THz timescale [50]. The implications of these results for the current system are beyond the scope of our work.

The intrinsic OHE. The consistency between our σ_{OH} and the value from first-principles calculations, and the scattering-independent orbital Hall conductivity, combine to suggest a dominant intrinsic OHE in V. In the study of the intrinsic versus extrinsic mechanisms of the anomalous Hall effect and the spin Hall effect, the common practice is to perform scaling analysis of the relevant Hall conductivity against σ_{xx} [51,52]. It has been shown that the scaling behavior of OHE can be distinct from the spin counterpart, especially in the strong-scattering regime: in $SrRuO_3$, σ_{OH} remains constant at high σ_{xx} but exhibits a striking enhancement as σ_{xx} decreases, contrasting with spin Hall effect suppression at low σ_{xx} [20]. In V, the intrinsic nature of the OHE was suggested by examining orbital transport using measurements spanning different timescales, from quasistatic to picoseconds [25]. However, observation of the scattering-independent orbital Hall conductivity has not been reported until now. In a previous study where the orbital transport parameters were determined from the Hanle magnetoresistance, a decrease of σ_{OH} with the decrease of σ_{xx} was observed, due to the relatively small σ_{xx} of the samples [48]. Our epitaxial growth of high-quality V films allows us to reach the clean regime, with a σ_{xx} one order larger than that in Ref. [48], where the intrinsic OHE dominates, and the scattering-independent scaling manifests. We note that in the scaling analysis presented in Fig. 7, we use the value of ξ/ρ_{xx} for V(10)/Ni(6) as a measure of the orbital Hall conductivity σ_{OH}. This might become inappropriate if λ_{orb} increases substantially with decreasing temperature, in which case ξ may only saturate to a higher value for thicker V. This would translate to an increasing σ_{OH} with decreasing temperature. Such an Elliott-Yafetlike σ_{OH} is, however, characteristic of the dirty limit [53], in contrast to the clean metal here.

V. CONCLUSION

The epitaxial growth of the films enables us to realize efficient orbital current generation in the light metal V. The orbital-to-spin current conversion is enabled by inserting a Pt layer between V and the ferromagnetic layer, or by using Ni as the ferromagnetic layer. Specifically for V/Ni, we determine from spin-torque ferromagnetic resonance measurements an orbital Hall conductivity $\sim 1.8 \times 10^3(\hbar/e)(\Omega\ \mathrm{cm})^{-1}$, and an orbital diffusion length ~5.38 nm. By injecting charge current at different angles relative to a crystallographic direction, we uncovered the isotropic nature of orbital current generation, consistent with the expectation for the orbital Hall effect in a cubic material. Benefiting from the low level of disorder in our high-quality V films, we were able to observe the scattering-independent scaling characteristic of the intrinsic orbital Hall effect.

ACKNOWLEDGMENTS

This work was supported by the National Natural Science Foundation of China (Grants No. 12574117, No. 12274125, and No. 12374105). The authors thank the Analytical and Testing Center of East China Normal University for technical support in XRD and AFM measurements.

DATA AVAILABILITY

The data that support the findings of this article are not publicly available upon publication because it is not technically feasible and/or the cost of preparing, depositing, and hosting the data would be prohibitive within the terms of this research project. The data are available from the authors upon reasonable request.

[1] I. Žutić, J. Fabian, and S. Das Sarma, Spintronics: Fundamentals and applications, Rev. Mod. Phys. **76**, 323 (2004).
[2] B. Dieny, I. L. Prejbeanu, K. Garello, P. Gambardella, P. Freitas, R. Lehndorff, W. Raberg, U. Ebels, S. O. Demokritov, J. Akerman, A. Deac, P. Pirro, C. Adelmann, A. Anane, A. V. Chumak, A. Hirohata, S. Mangin, S. O. Valenzuela, M. C. Onbaşlı, M. d'Aquino, *et al.*, Opportunities and challenges for spintronics in the microelectronics industry, Nat. Electron. **3**, 446 (2020).
[3] A. Manchon, J. Železný, I. M. Miron, T. Jungwirth, J. Sinova, A. Thiaville, K. Garello, and P. Gambardella, Current-induced spin-orbit torques in ferromagnetic and antiferromagnetic systems, Rev. Mod. Phys. **91**, 035004 (2019).
[4] X. Han, X. Wang, C. Wan, G. Yu, and X. Lv, Spin-orbit torques: Materials, physics, and devices, Appl. Phys. Lett. **118**, 120502 (2021).
[5] G. Ji, Y. Zhang, Y. Chai, and T. Nan, Recent progress on controlling spin-orbit torques by materials design, npj Spintron. **2**, 56 (2024).
[6] L. Šmejkal, J. Sinova, and T. Jungwirth, Emerging research landscape of altermagnetism, Phys. Rev. X **12**, 040501 (2022).
[7] C. Song, H. Bai, Z. Zhou, L. Han, H. Reichlova, J. H. Dil, J. Liu, X. Chen, and F. Pan, Altermagnets as a new class of functional materials, Nat. Rev. Mater. **10**, 473 (2025).
[8] C. Cao, S. Chen, R.-C. Xiao, Z. Zhu, G. Yu, Y. Wang, X. Qiu, L. Liu, T. Zhao, D.-F. Shao, Y. Xu, J. Chen, and Q. Zhan, Anomalous spin current anisotropy in a noncollinear antiferromagnet, Nat. Commun. **14**, 5873 (2023).
[9] D. Jo, D. Go, G.-M. Choi, and H.-W. Lee, Spintronics meets orbitronics: Emergence of orbital angular momentum in solids, npj Spintron. **2**, 19 (2024).
[10] P. Wang, F. Chen, Y. Yang, S. Hu, Y. Li, W. Wang, D. Zhang, and Y. Jiang, Orbitronics: Mechanisms, materials and devices, Adv. Electron. Mater. **11**, 2400554 (2025).
[11] S. Fukami, K.-J. Lee, and M. Kläui, Challenges and opportunities in orbitronics, Nat. Phys. **22**, 999 (2026).
[12] T. Gao, P. Rüßmann, Q. Wang, R. Fukunaga, H. Hayashi, D. Go, T. Harumoto, R. Tu, S. Zhang, L. Zhang, Y. Mokrousov, J. Shi, and K. Ando, Control of dynamic orbital response in ferromagnets via crystal symmetry, Nat. Phys. **20**, 1896 (2024).
[13] H. Hayashi, J. Chen, D. Jo, S. Sakamoto, T. Gao, D. Go, Y. Mokrousov, H.-W. Lee, S. Miwa, and K. Ando, Crystallographic engineering for enhanced orbital torque, Nano Lett. **25**, 15124 (2025).
[14] H. Lee, B. Choi, and H.-W. Lee, Orientational dependence of intrinsic orbital and spin Hall effects in hcp structure materials, Phys. Rev. B **105**, 035142 (2022).
[15] R. Xiao, T. Zhao, I. Baek, H. Lee, Z. Zheng, S. Shi, Z. Xie, Q. Zhang, L. Jia, P. Yang, X. Yu, D. Song, H.-W. Lee, and J. Chen, Crystal symmetry-dependent orbital Rashba-Edelstein effect in epitaxial CuO thin film, Nat. Commun. **17**, 4461 (2026).
[16] A. El Hamdi, J.-Y. Chauleau, M. Boselli, C. Thibault, C. Gorini, A. Smogunov, C. Barreteau, S. Gariglio, J.-M. Triscone, and M. Viret, Observation of the orbital inverse Rashba-Edelstein effect, Nat. Phys. **19**, 1855 (2023).
[17] Y.-G. Choi, D. Jo, K.-H. Ko, D. Go, K.-H. Kim, H. G. Park, C. Kim, B.-C. Min, G.-M. Choi, and H.-W. Lee, Observation of the orbital Hall effect in a light metal Ti, Nature (London) **619**, 52 (2023).

[18] H. Liu and D. Culcer, Dominance of extrinsic scattering mechanisms in the orbital Hall effect: Graphene, transition metal dichalcogenides, and topological antiferromagnets, Phys. Rev. Lett. **132**, 186302 (2024).

[19] A. Veneri, T. G. Rappoport, and A. Ferreira, Extrinsic orbital Hall effect: Orbital skew scattering and crossover between diffusive and intrinsic orbital transport, Phys. Rev. Lett. **134**, 136201 (2025).

[20] S. Peng, X. Zheng, S. Li, B. Lao, Y. Han, Z. Liao, H. Zheng, Y. Yang, T. Yu, P. Liu, Y. Sun, X.-Q. Chen, S. Peng, W. Zhao, R.-W. Li, and Z. Wang, Unconventional scaling of the orbital Hall effect, Nat. Mater. **24**, 1749 (2025).

[21] D. Jo, D. Go, and H.-W. Lee, Gigantic intrinsic orbital Hall effects in weakly spin-orbit coupled metals, Phys. Rev. B **98**, 214405 (2018).

[22] Q. Guo, Z. Ren, H. Bai, X. Wang, G. Yu, W. He, J. Teng, and T. Zhu, Current-induced magnetization switching in perpendicularly magnetized V/CoFeB/MgO multilayers, Phys. Rev. B **104**, 224429 (2021).

[23] X. Liu, F. Liu, and C. Jiang, Harnessing orbital Hall effect for efficient orbital torque in light metal vanadium, J. Magn. Magn. Mater. **610**, 172585 (2024).

[24] M. X. Aguilar-Pujol, I. C. Arango, E. Dolan, Y. Ba, M. Gobbi, L. E. Hueso, and F. Casanova, Orbital Hall conductivity and orbital diffusion length of vanadium thin films by Hanle magnetoresistance, Newton **1**, 100290 (2025).

[25] N. Vijayan, D. Kumar, A. Du, M. Sastges, L. Gao, Z. Xiao, D. Go, J. O. Ledesma-Martin, H. I. Wang, D. Jo, P. M. Oppeneer, R. Gupta, G. Jakob, S. Krishnia, Y. Mokrousov, and M. Kläui, Itinerant orbital Hall effect mechanism leading to large negative orbital torques from light metal vanadium, arXiv:2508.16339.

[26] S. Lee, M.-G. Kang, D. Go, D. Kim, J.-H. Kang, T. Lee, G.-H. Lee, J. Kang, N. J. Lee, Y. Mokrousov, S. Kim, K.-J. Kim, K.-J. Lee, and B.-G. Park, Efficient conversion of orbital Hall current to spin current for spin-orbit torque switching, Commun. Phys. **4**, 234 (2021).

[27] D. Lee, D. Go, H.-J. Park, W. Jeong, H.-W. Ko, D. Yun, D. Jo, S. Lee, G. Go, J. H. Oh, K.-J. Kim, B.-G. Park, B.-C. Min, H. C. Koo, H.-W. Lee, O. Lee, and K.-J. Lee, Orbital torque in magnetic bilayers, Nat. Commun. **12**, 6710 (2021).

[28] Y. Xie, Q. Zhan, Y. Hu, X. Hu, X. Chi, C. Zhang, H. Yang, W. Xie, X. Zhu, J. Gao, W. Cheng, D. Jiang, and R.-W. Li, Magnetocrystalline anisotropy imprinting of an antiferromagnet on an amorphous ferromagnet in FeRh/CoFeB heterostructures, NPG Asia Mater. **12**, 67 (2020).

[29] L. Liu, T. Moriyama, D. C. Ralph, and R. A. Buhrman, Spin-torque ferromagnetic resonance induced by the spin Hall effect, Phys. Rev. Lett. **106**, 036601 (2011).

[30] A. Bose, F. Kammerbauer, R. Gupta, D. Go, Y. Mokrousov, G. Jakob, and M. Kläui, Detection of long-range orbital-Hall torques, Phys. Rev. B **107**, 134423 (2023).

[31] A. M. Gonçalves, I. Barsukov, Y.-J. Chen, L. Yang, J. A. Katine, and I. N. Krivorotov, Spin torque ferromagnetic resonance with magnetic field modulation, Appl. Phys. Lett. **103**, 172406 (2013).

[32] J.-W. Xu and A. D. Kent, Charge-to-spin conversion efficiency in ferromagnetic nanowires by spin torque ferromagnetic resonance: Reconciling lineshape and linewidth analysis methods, Phys. Rev. Appl. **14**, 014012 (2020).

[33] S. Karimeddiny and D. C. Ralph, Resolving discrepancies in spin-torque ferromagnetic resonance measurements: Lineshape versus linewidth analyses, Phys. Rev. Appl. **15**, 064017 (2021).

[34] C.-F. Pai, Y. Ou, L. H. Vilela-Leão, D. C. Ralph, and R. A. Buhrman, Dependence of the efficiency of spin Hall torque on the transparency of Pt/ferromagnetic layer interfaces, Phys. Rev. B **92**, 064426 (2015).

[35] J. Bass and W. P. Pratt, Spin-diffusion lengths in metals and alloys, and spin-flipping at metal/metal interfaces: An experimentalist's critical review, J. Phys.: Condens. Matter **19**, 183201 (2007).

[36] W. Zhang, V. Vlaminck, J. E. Pearson, R. Divan, S. D. Bader, and A. Hoffmann, Determination of the Pt spin diffusion length by spin-pumping and spin Hall effect, Appl. Phys. Lett. **103**, 242414 (2013).

[37] G. Sala and P. Gambardella, Giant orbital Hall effect and orbital-to-spin conversion in $3d$, $5d$, and $4f$ metallic heterostructures, Phys. Rev. Res. **4**, 033037 (2022).

[38] E. M. Chudnovsky, Intrinsic spin Hall effect in noncubic crystals, Phys. Rev. B **80**, 153105 (2009).

[39] F. Freimuth, S. Blügel, and Y. Mokrousov, Anisotropic spin Hall effect from first principles, Phys. Rev. Lett. **105**, 246602 (2010).

[40] M.-H. Nguyen, D. C. Ralph, and R. A. Buhrman, Spin torque study of the spin Hall conductivity and spin diffusion length in platinum thin films with varying resistivity, Phys. Rev. Lett. **116**, 126601 (2016).

[41] H. Moriya, M. Taniguchi, D. Jo, D. Go, N. Soya, H. Hayashi, Y. Mokrousov, H.-W. Lee, and K. Ando, Observation of long-range current-induced torque in Ni/Pt bilayers, Nano Lett. **24**, 6459 (2024).

[42] Q. Liu and L. Zhu, Absence of orbital current torque in Ta/ferromagnet bilayers, Nat. Commun. **16**, 8660 (2025).

[43] Y. Marui, M. Kawaguchi, S. Sumi, H. Awano, K. Nakamura, and M. Hayashi, Spin and orbital Hall currents detected via current-induced magneto-optical Kerr effect in V and Pt, Phys. Rev. B **108**, 144436 (2023).

[44] E. Lesne, Y. Fu, S. Oyarzun, J. C. Rojas-Sánchez, D. C. Vaz, H. Naganuma, G. Sicoli, J.-P. Attané, M. Jamet, E. Jacquet, J.-M. George, A. Barthélémy, H. Jaffrès, A. Fert, M. Bibes, and L. Vila, Highly efficient and tunable spin-to-charge conversion through Rashba coupling at oxide interfaces, Nat. Mater. **15**, 1261 (2016).

[45] D. C. Vaz, P. Noël, A. Johansson, B. Göbel, F. Y. Bruno, G. Singh, S. McKeown-Walker, F. Trier, L. M. Vicente-Arche, A. Sander, *et al.*, Mapping spin-charge conversion to the band structure in a topological oxide two-dimensional electron gas, Nat. Mater. **18**, 1187 (2019).

[46] T. Tanaka, H. Kontani, M. Naito, T. Naito, D. S. Hirashima, K. Yamada, and J. Inoue, Intrinsic spin Hall effect and orbital Hall effect in $4d$ and $5d$ transition metals, Phys. Rev. B **77**, 165117 (2008).

[47] I. Lyalin, S. Alikhah, M. Berritta, P. M. Oppeneer, and R. K. Kawakami, Magneto-optical detection of the orbital Hall effect in chromium, Phys. Rev. Lett. **131**, 156702 (2023).

[48] G. Sala, H. Wang, W. Legrand, and P. Gambardella, Orbital Hanle magnetoresistance in a $3d$ transition metal, Phys. Rev. Lett. **131**, 156703 (2023).

[49] M. Rang and P. J. Kelly, Orbital relaxation length from first-principles scattering calculations, Phys. Rev. B **109**, 214427 (2024).

[50] T. Guan, J. Liu, W. Qin, Y. Cui, S. Wang, Y. Wu, and Z. Tao, Evidences of subnanometre orbital diffusion length in heavy metals using terahertz emission spectroscopy, Nat. Nanotechnol. **21**, 538 (2026).

[51] N. Nagaosa, J. Sinova, S. Onoda, A. H. MacDonald, and N. P. Ong, Anomalous Hall effect, Rev. Mod. Phys. **82**, 1539 (2010).

[52] D. Hou, G. Su, Y. Tian, X. Jin, S. A. Yang, and Q. Niu, Multivariable scaling for the anomalous Hall effect, Phys. Rev. Lett. **114**, 217203 (2015).

[53] J. Sinova, S. O. Valenzuela, J. Wunderlich, C. H. Back, and T. Jungwirth, Spin Hall effects, Rev. Mod. Phys. **87**, 1213 (2015).